AIAA-2000-0139

Unsteady Slat-Wake Characteristics of a High-Lift Configuration

K. Paschal, L. Jenkins, and C. Yao
NASA LaRC
Hampton, VA

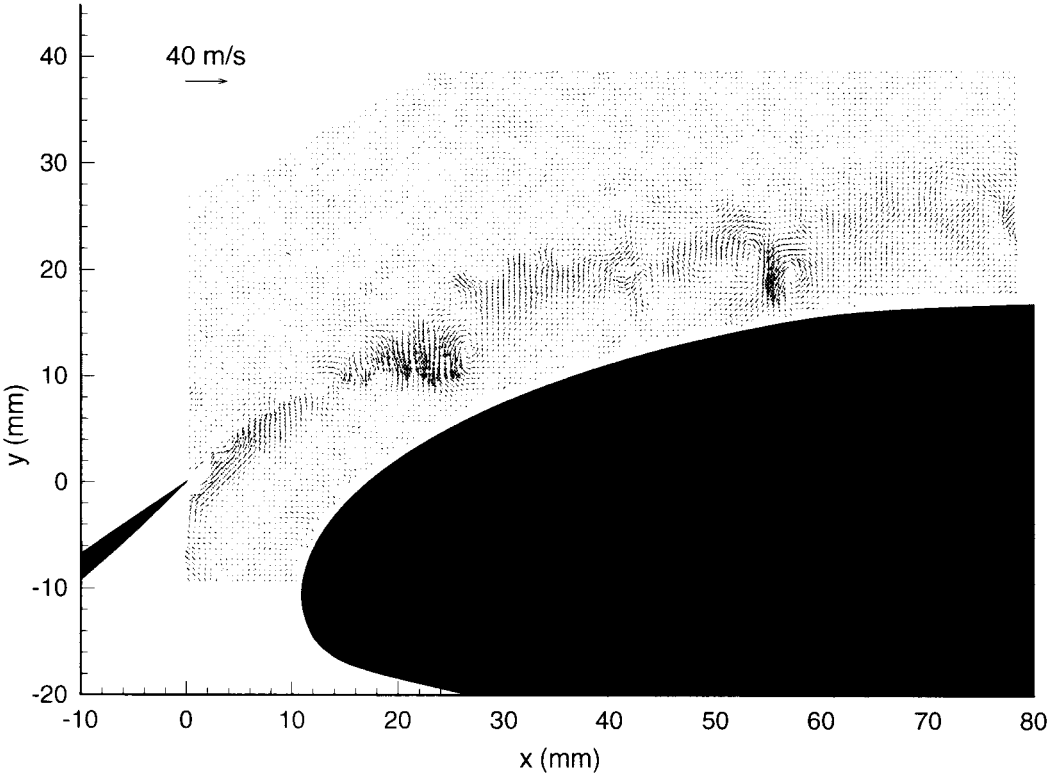

38th Aerospace Sciences Meeting & Exhibit
10-13 January 2000 / Reno, NV

UNSTEADY SLAT WAKE CHARACTERISTICS OF A 2-D HIGH-LIFT CONFIGURATION

Keith Paschal*, Luther Jenkins*, and Chungsheng Yao*
NASA Langley Research Center
Hampton, VA

Abstract

Unsteady characteristics of the slat wake associated with a three-element high-lift model were investigated with Particle Image Velocimetry (PIV). The test was conducted in the NASA Langley Basic Aerodynamic Research Tunnel (BART) employing sidewall blowing to maintain 2-D flow over the high-lift configuration. The main goal of the experiment was to document spatial characteristics of the unsteady slat wake in an effort to further guide computational efforts. PIV measurements were made at 4, 8, and 10 degrees angle of attack. Instantaneous vector maps revealed organized structures that had been ejected from the slat cove merging with the slat wake. This phenomenon is attributed to the unsteadiness of the recirculation region in the slat cove. The unsteadiness is most pronounced at 4 degrees. Mean data show a wide, diffuse wake at 4 degrees that becomes both narrow and well defined at 10 degrees angle of attack. Second-order statistics suggest a similar trend. These statistics show higher levels of fluctuations due to slat cove unsteadiness and turbulence at 4 degrees, while the slat cove flow has apparently stabilized at the higher angles of attack.

Symbols

α	angle of attack
C_p	coefficient of pressure
δ_f	flap deflection
δ_s	slat deflection
M	Mach number
η	surface normal direction
R_c	Reynolds number based on chord
U_s	velocity magnitude
u',v'	fluctuating and unsteady velocity components, tunnel reference frame
$\langle v'^2 \rangle / U^2$	wall-normal stress
x/c	non-dimensional streamwise direction
z/s	non-dimensional spanwise direction

Introduction

Prediction of the 2-D, high-lift flow field is still unreliable despite recent advances in the computational field. A joint NASA - Boeing workshop was held in 1996 to address issues related to accuracy of CFD high-lift predictions. A research program was laid out in order to address both the effect of transition location and turbulence model on the accuracy of the computational predictions. One of the findings was that transition location and code implementation played a key role in accurately predicting the flow-field[1].

Regardless of code transition implementation, the codes still exhibit an inability to correctly predict the wakes of both the slat and main element at relevant flight angles-of-attack. A series of measurements were made in the NASA Langley Low-Turbulence Pressure Tunnel (LTPT) on the McDonnell Douglas Aircraft (MDA) high-lift configuration to provide reliable comparison data[2]. Hot-wire measurements in the slat wake at $\alpha = 4$ and 8° revealed unsteadiness presumably arising from the slat cove. The goal of the present investigation was to look more closely at the details of the slat wake in the BART facility using PIV as a means to quantitatively measure and document the effects of slat cove unsteadiness.

Experiment

The experiment was conducted in the NASA Langley Basic Aerodynamic Research Tunnel (BART). The tunnel has a cross-sectional area of 1.016 m by 0.711 m and maximum speed of 60 m/s. The three-element Douglas (MDA) high-lift model had previously been

* Aerospace Engineer, Flow Physics and Control Branch

tested in a study that eliminated massive flap separation using micro-vortex generators[3]. In both cases the model was mounted between tunnel sidewalls spanning the width of the tunnel. Also, the MDA geometry (figures 1 and 2) has been widely used in computational studies as well as experiments in the LTPT[4,5]. The PIV measurement region relative to the model geometry is shown in figure 2. The MDA model has a nested chord of 457.2 mm and is equipped with chordwise and spanwise pressure taps. The high-lift configuration tested was the commonly known 30P-30N configuration. 30P refers to the slat deflection (δ_s=-30°) and overhang-gap location relative to the main element. 30N refers to the same parameters on the flap (δ_f=30°). 30P-30N is considered to be a relatively clean flow configuration. Measurements were made at R_c = 1.5 million, M = 0.15, and α = 4, 8, and 10°.

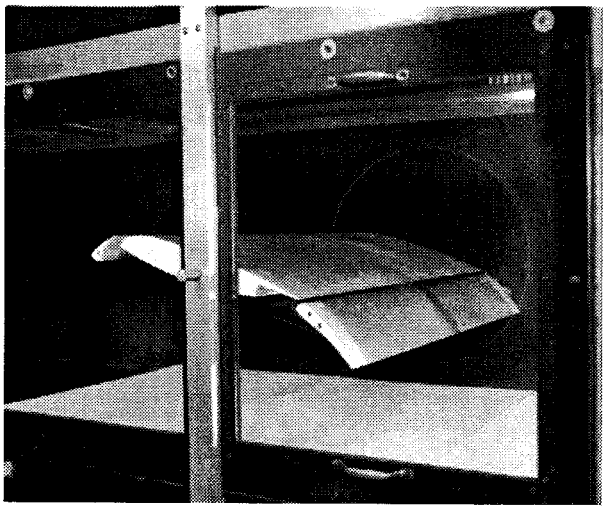

Figure 1. Photo of MDA model in BART (α = 8°).

To ensure spanwise uniformity of the flow field, some form of tunnel sidewall boundary layer control is required. Large adverse pressure gradients induced by the high-lift airfoil can cause tunnel sidewall boundary layer separation[6]. In an effort to maintain 2-D flow over the model blowing tubes were positioned tangentially at approximately 15% of the flap chord and connected to shop air regulated at 80 psi. Spanwise pressure measurements made near the trailing edges of both the main element and flap confirm that 2-D flow was achieved (figure 3). The worst case scenario (α = 10°) has been shown in figure 3. Pressure measurements were made using an ESP system accurate to +/- 0.045% of full scale. Once 2-D flow was achieved, smoke flow visualization was performed to ensure that the model was not inducing tunnel floor or ceiling boundary layer separation. Oil flow (titanium dioxide and kerosene) was also used to confirm 2-D flow over the model by checking surface streamlines.

Transition locations on the MDA model needed to be determined if there were to be any future hope of reconciling these data with computations. Sublimating chemicals were used in an attempt to qualitatively estimate the transition location on each of the three elements[7]. The model surface was treated with Naphthalene (mothballs), which would sublimate at a rate based on the heat transfer between the boundary layer and the model surface. When preformed properly, a turbulent boundary layer would cause the sublimation of Naphthalene, while a laminar boundary layer would not. Laminar flow was seen over the entire slat, while the boundary layers over the main element and flap apparently tripped at their respective suction peak locations (figure 4). Our investigation revealed, as did Klausmeyer's[3], possible separation bubbles near the leading edges of both the main element and the flap.

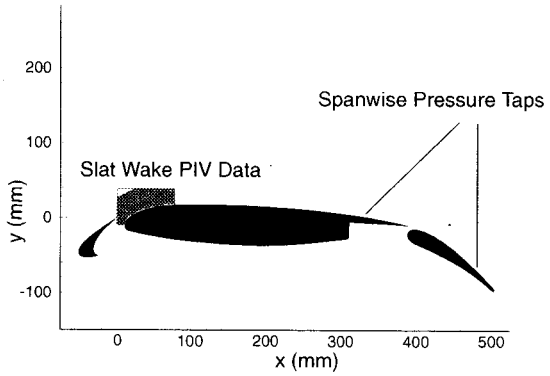

Figure 2. Instantaneous PIV vector map relative to the MDA geometry (α = 4°).

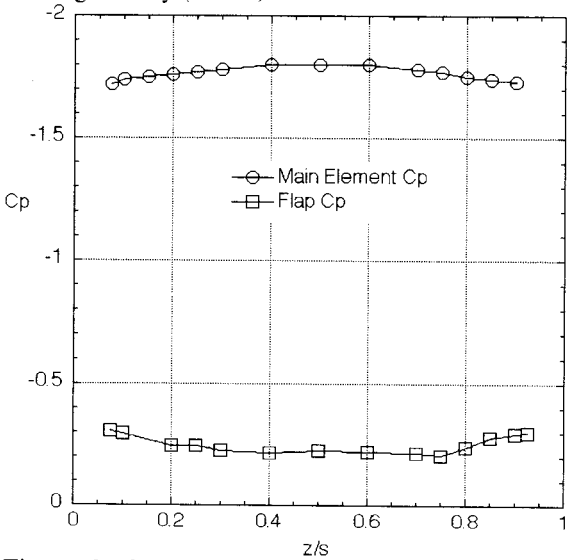

Figure 3. Confirmation of 2-D flow from spanwise pressure measurements at α = 10°.

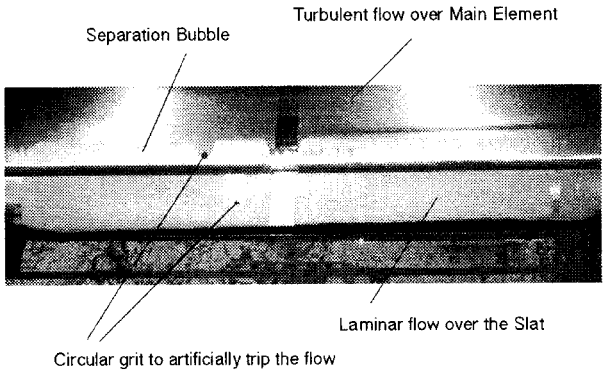

Figure 4. Boundary layer state information over the slat and main-element leading edge ($\alpha = 8^\circ$).

PIV is an optical technique used to acquire planar velocity measurements at a single moment in time. Double exposures of micron sized particles are imaged, and correlations are computed to determine average particle displacements. A film-based image acquisition system was used to satisfy the strict requirement of large field of view versus small spatial resolution. These are typical requirements in turbulent flows. A detailed description of our system is given in Yao and Paschal[8], and a good overview of the technique in general can be found in Adrian's review paper[9]. Our film-based system, which was used in the present experiment, provided a spatial resolution of 1 mm over a field of view of 80 mm in the streamwise direction. Approximately 150 instantaneous realizations were acquired at each angle of attack.

The PIV system employs two Nd:YAG lasers, each providing over 500 mJ of energy. The beams are combined, aligned, and formed into a light sheet that is directed into the tunnel test section. A Cambo 4" by 5" camera with a Rodenstock 1:1 lens is used to image the particles. A calcite crystal was placed in front of the lens to artificially shift the second image exposure and thus remove flow direction ambiguity. Seeding was accomplished using TSI 6-jet atomizers producing a polydispersed distribution with a mean diameter less than 1 micron. Despite the polydispersed distribution, 99% of all particles were less than 2 microns. Particle lag was less then 5% based on particle slip velocity as a function of applied acceleration[9].

Results

Chordwise pressure distributions for the three angles of attack are shown in figures 5, 6, and 7. The flap pressures are unchanged throughout the angle of attack range as the main element helps to regulate the flow field over the flap. The flap is tucked slightly under the trailing edge of the main element (figure 2) for this particular gap-overhang setting. The slat is initially unloaded at $\alpha = 4^\circ$, and only modestly loaded at $\alpha = 10^\circ$. The flow field over the slat and main element is highly dependent upon configuration angle of attack as well as gap-overhang settings.

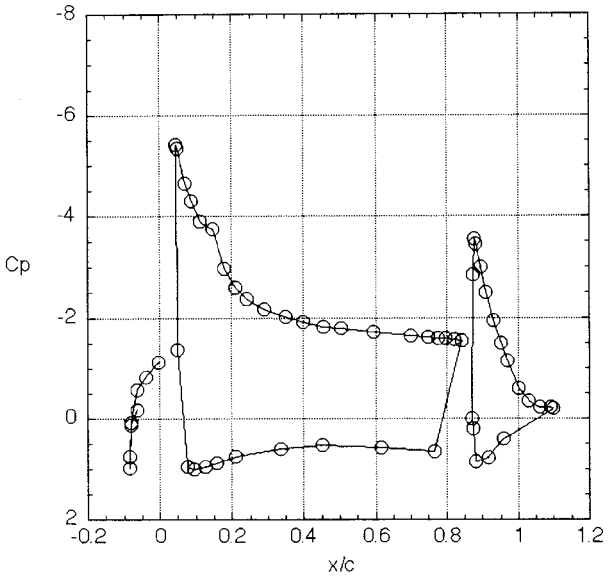

Figure 5. Chordwise pressure distributions $\alpha = 4^\circ$.

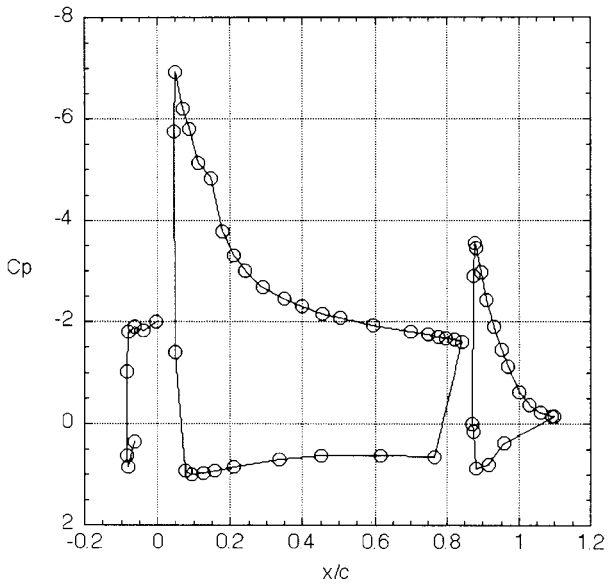

Figure 6. Chordwise pressure distributions $\alpha = 8^\circ$.

Fluctuating vector maps were computed by subtracting the average of all the realizations from each individual realization. Two spanwise vortex structures that have emerged from the slat cove can be seen in figure 8 (x ~ 25 mm and x ~ 55 mm). The probability of occurrence

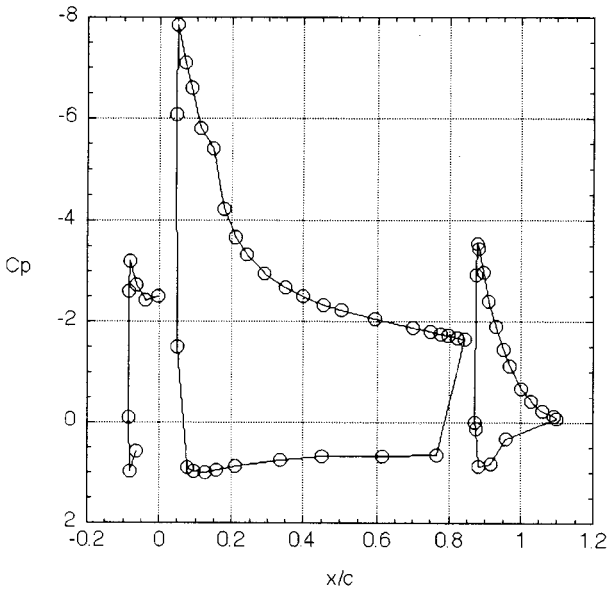

Figure 7. Chordwise pressure distributions $\alpha = 10^{\circ}$.

of these structures is much greater at 4° presumably due to slat cove unsteadiness. Figure 9 is indicative of a streamwise vortex probably emanating from the slat cove, while figure 10 depicts a fairly quiet wake without the unsteady effects from the slat cove. Data shown in the three figures were acquired at $\alpha = 4^{\circ}$. The fluctuating maps at higher angles of attack showed less vigorous activity on average, and lower numbers of unsteady events. McGinley et al.[2] also observed unsteady events at low angles of attack with a single-wire hotwire in the slat wake of the MDA configuration at R_c = 9 million. Those unsteady events also vanished at the higher angles of attack.

Structures similar to those seen in figures 8 and 9 were pseudo-quantified using spatial scale and strength intensity. The spanwise rollers seen in figure 8 have a spatial scale on the order of at least 5 mm. This is a fairly typical value based on observation of the entire data set. Depending on the downstream extent of wake development, this scale is on the order of the wake thickness, if not greater. The intensity of the instantaneous fluctuations seen in figure 9 are an order of magnitude stronger than the statistical average obtained from the wall-normal stress ($\langle v'^2 \rangle / U^2$). Events observed in the wake matching these two criteria were deemed to have originated in the unsteady slat cove flow field.

Approximately 150 instantaneous realizations were used to compute the mean flow at each angle of attack. Figure 11 shows the mean profiles at x/c = 0.10 where η is the surface normal. At $\alpha = 4$ and 8° the wake is wide and disorganized with weak gradients. Since the slat is not highly loaded at $\alpha = 4^{\circ}$, one would expect a somewhat smaller wake deficit. However, the broadened asymmetric lower edge of the wake indicates that unsteady events, presumably from the slat cove, are influencing the slat wake. Only at $\alpha = 10^{\circ}$ does a more standard wake structure appear with reasonable gradients and narrow region of mass flow deficit. These profiles are very similar to measurements made by McGinley et al.[2] in the Langley LTPT (figure 12).

PIV second order moments are a measure of both slat wake turbulence and flow unsteadiness. The spatial distribution of the normalized wall-normal stress can be seen in the contour maps shown in figures 13 and 14 for $\alpha = 4^{\circ}$ and 10°. The normal and shearing stresses were computed in the tunnel frame of reference. The stress components were computed from approximately 150 instantaneous PIV realizations. They are good estimators of the second order moments, though not yet fully converged

If one assumes turbulence production to scale with mean gradient strength, from observation of the mean profiles one would expect the largest stress values to occur $\alpha = 10^{\circ}$ (figure 11). This is not the case. The larger stress magnitudes occur at the lower angle of attack, and therefore do not correlate with the relatively weaker mean gradients at that condition. However, the spatial extent or distribution of the wall normal stress does correlate with the wake width seen in the mean profiles (refer to figures 11, 13, 14). This observation suggests that the increased turbulence and unsteadiness is emanating from somewhere other than the slat wake, namely the slat cove. The strong, thick shear layer emerging from the slat cove can be clearly seen in figure 13. By comparison, a relatively narrow stress band is observed at $\alpha = 10^{\circ}$.

The final analysis performed was a mean computation based on a conditional average. The individual realizations were divided into two categories, events and non-events. An event was deemed to be an unsteady structure as previously defined based on spatial scale and fluctuating intensity. Examples of events have been shown in figures 8 and 9 where streamwise and spanwise structures are seen to exist. Large discrepancies are seen to exist at $\alpha = 4^{\circ}$ between the event and non-event profiles at x/c = 0.10 (figure 15). While the unsteady component does not completely explain the wide, disorganized wake and associated weak gradients, the effect is clearly important. At $\alpha = 10^{\circ}$ the discrepancy between event and non-event profile is less pronounced but still evident. Approximately 61% of the realizations at $\alpha =$

4° showed signs of unsteady events, while this value dropped to 38% at $\alpha = 10°$. The unsteady components associated with the local flow field of the slat cove play a large role at $\alpha = 4°$ and are still important up to $\alpha = 10°$.

Conclusions

PIV measurements made in the slat wake of the MDA 30P-30N high-lift configuration show significant flow unsteadiness in the slat wake. Conditional averaging based on the existence or non-existence of unsteady flow structures has shown the result to be a disorganized wake with weak gradients at low angles of attack. Similar trends were observed at near flight Reynolds Numbers in the Langley LTPT. The significance of this finding is not clear with respect to performance issues at Flight Reynolds numbers. Certainly the local flow field of the slat is affected, and one may deduce that transition over the slat and slat cove unsteadiness must be addressed before accurate computations may be performed on this configuration at low angles of attack regardless of Reynolds number.

References

1. Rumsey, C.L., Gatski, T.B., Ying, S.X., and Bertelrud, A., "Prediction of High-Lift Flows Using Turbulent Closure Models", AIAA 97-2260, June 1997.
2. McGinley, C.B., Anders, J.B., Spaid, F.W., "Measurements of Reynolds Stress Profiles on a High-Lift Airfoil", AIAA-98-2620, 1998.
3. Klausmeyer, S.M., Papadakis, M., Lin, J.C., "A Flow Physics Study of Vortex Generators on A Multi-Element Airfoil", AIAA 96-0548, January 1996.
4. Valarezo, W.O., Dominik, C.J., McGhee R.J., Goodman, W.L., Paschal, K.B., "Multi-Element Airfoil Optimization For Maximum Lift at High Reynolds Numbers", AIAA-91-3332-CP, 1991.
5. Klausmeyer, S.M., Lin, J.C., "Comparative Results From a CFD Challenge Over a 2D Three-Element High-Lift Airfoil, NASA TM 112858, May 1997.
6. Paschal, K., Goodman, W., McGhee, R., Walker, B., Wilcox, P., "Evaluation of Tunnel Sidewall Boundary-Layer-Control Systems for High-Lift Arifoil Testing", AIAA-91-3243, September 1991.
7. Obara, C.J., "Sublimating Chemical Technique for Boundary-Layer Flow Visualization in Flight Testing", Journal of Aircraft, Vol. 25, Num. 6, Pgs. 493-498, June 1988.
8. Yao, C., Paschal, K., "PIV Measurements of Airfoil Wake-Flow Turbulence Statistics and Turbulent Structures", AIAA-94-0085, January 1994.
9. Adrian, R.J., "Particle-Imaging Techniques For Experimental Fluid Mechanics", Annual Review of Fluid Mechanics, 23, pgs 261-304, 1991.

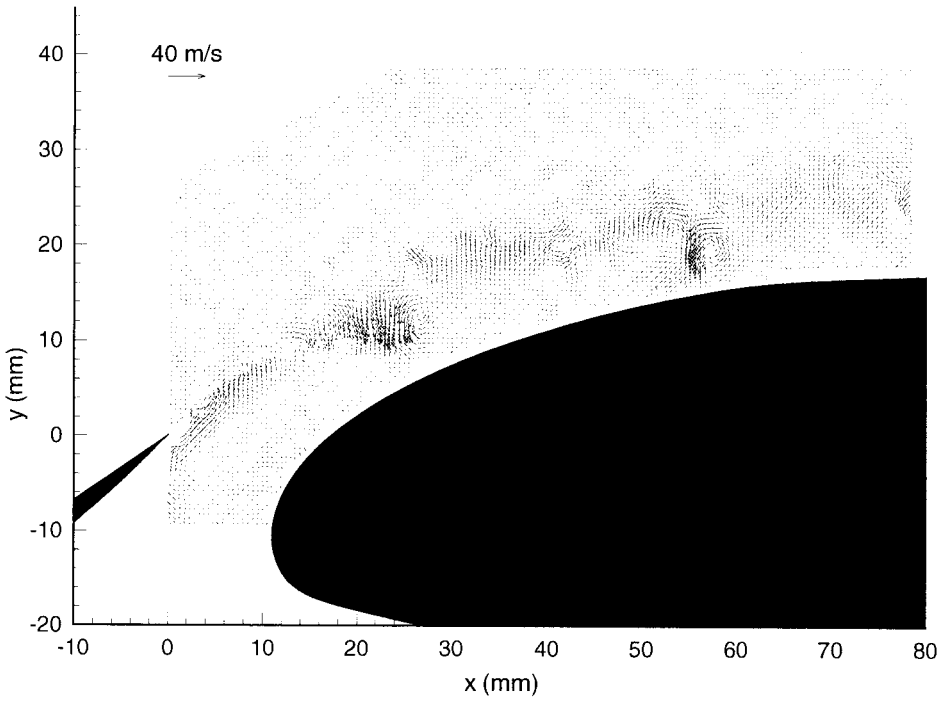

Figure 8. Instantaneous PIV realization $\alpha = 4^\circ$ (time t_1).

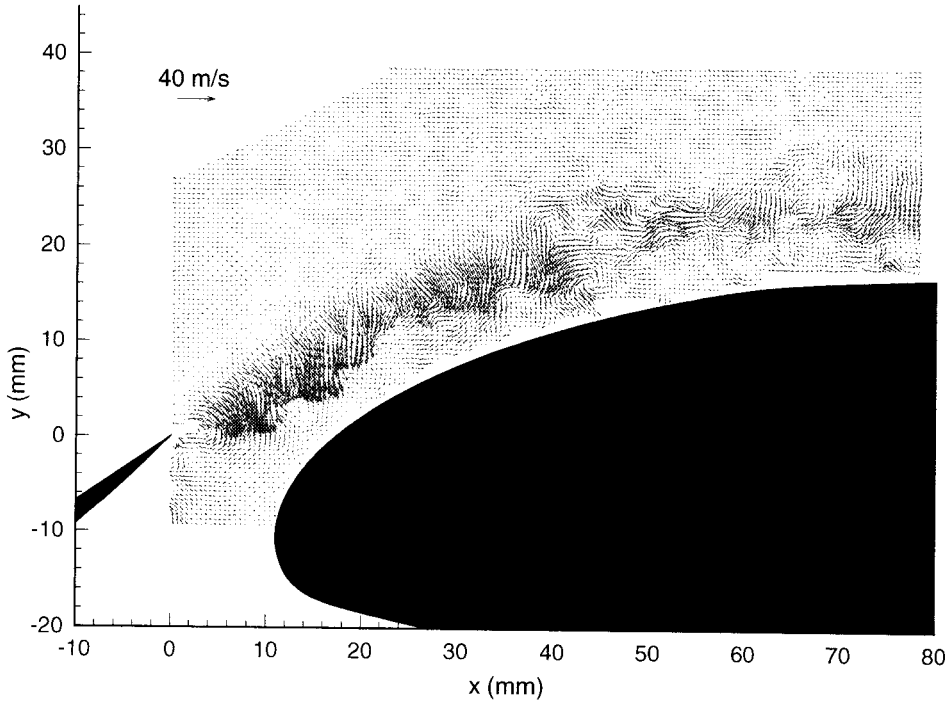

Figure 9. Instantaneous PIV realization $\alpha = 4^\circ$ (time t_2).

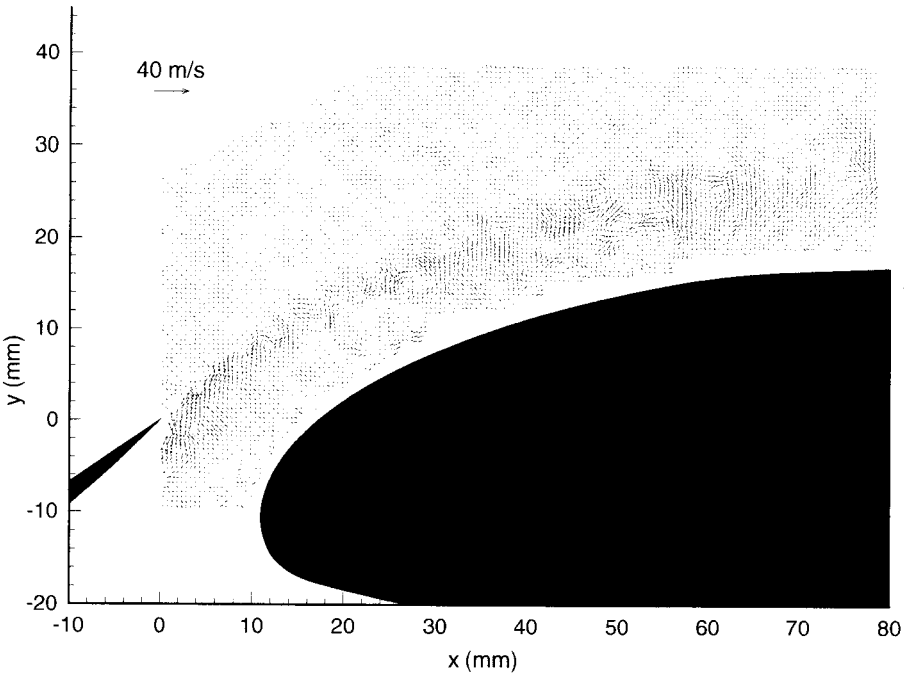

Figure 10. Instantaneous PIV realization $\alpha = 4^\circ$ (time t_3).

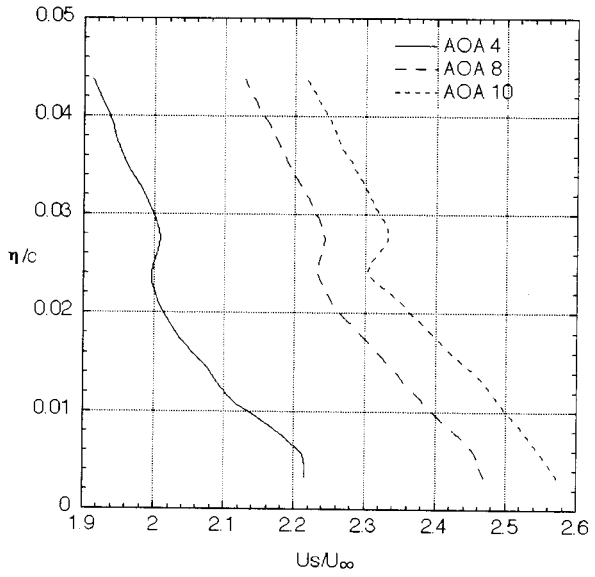

Figure 11. BART Mean profiles at x/c = 0.10.

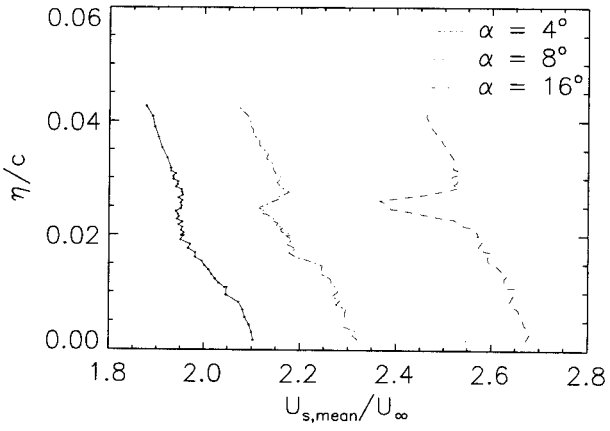

Figure 12. LTPT Mean profiles at x/c = 0.10.

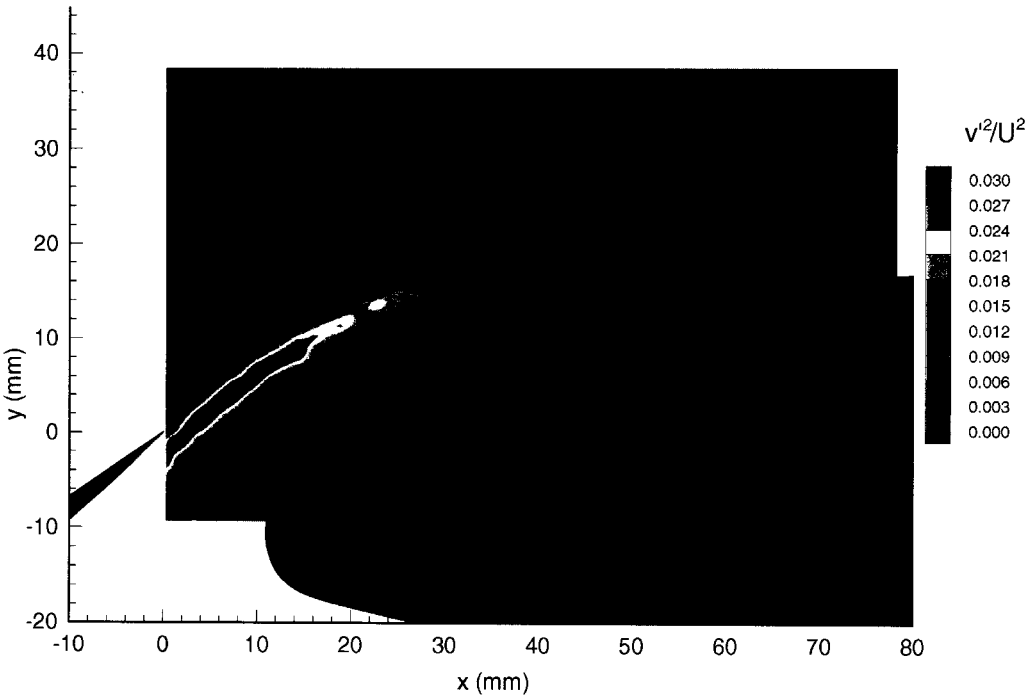

Figure 13. Normalized wall normal stress at $\alpha = 4°$.

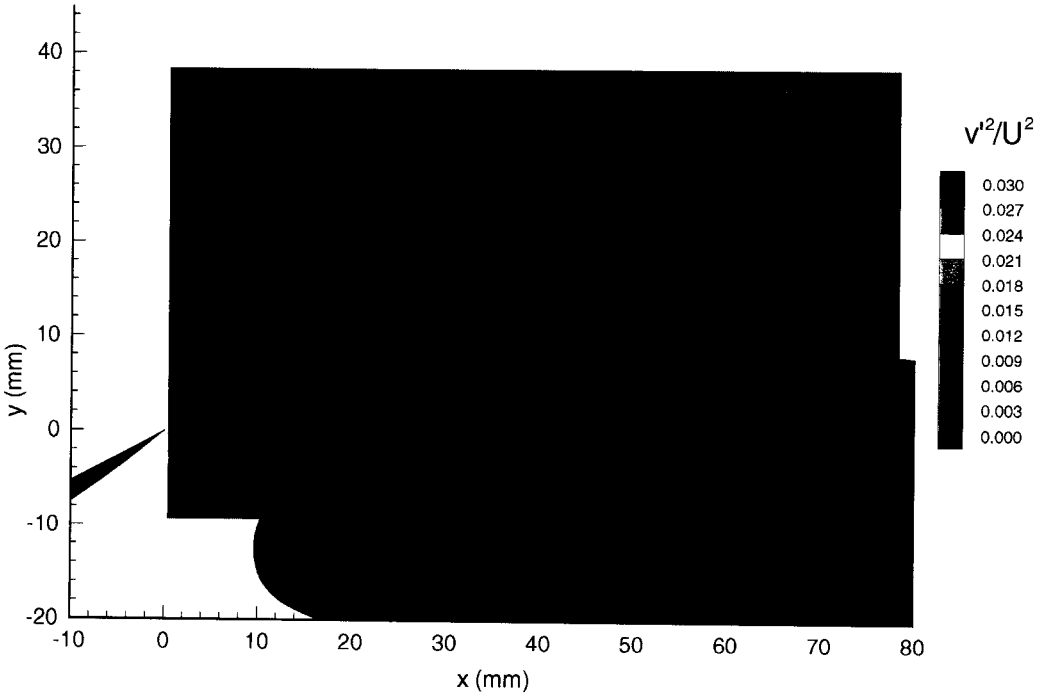

Figure 14. Normalized wall normal stress at $\alpha = 10°$.

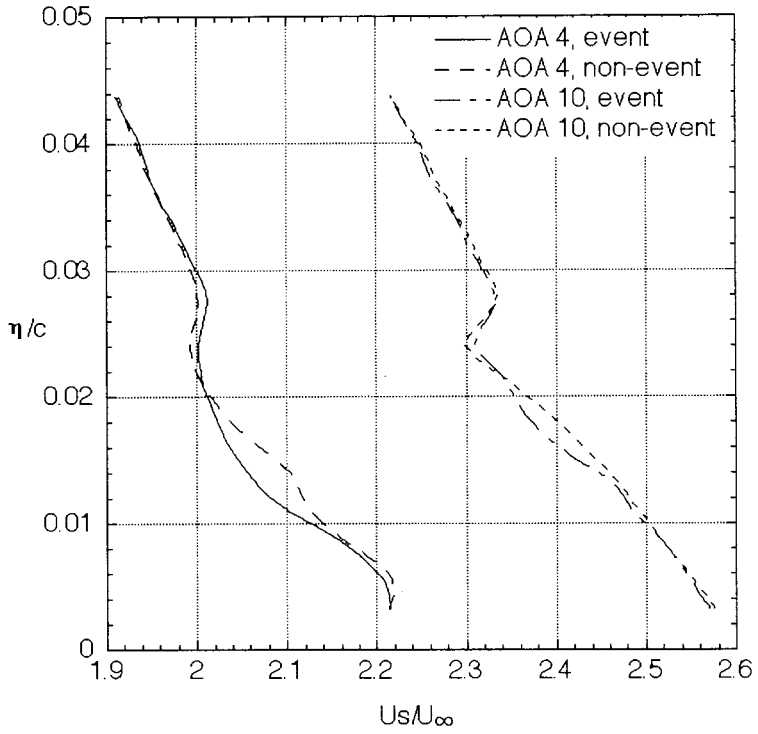

Figure 15. Conditionally averaged mean profiles at x/c = 0.10.